

ON THE RELATION BETWEEN MAGNETIC FIELD STRENGTH AND GAS DENSITY IN THE INTERSTELLAR MEDIUM. II. DENSITY UNCERTAINTIES AND DIFFUSE GAS CONSTRAINTS

DAVID WHITWORTH¹, AMIT SETA², RALPH E. PUDRITZ³, MORDECAI-MARK MAC LOW⁴, JUAN D. SOLER⁵, AINA PALAU⁶, RALF S. KLESSEN^{7,8}

¹ENS de Lyon, CRAL UMR5574, Universite Claude Bernard Lyon 1, CNRS, Lyon 69007, France

²Research School of Astronomy and Astrophysics, Australian National University, Canberra, ACT 2611, Australia

³Department of Physics and Astronomy, McMaster University, 1280 Main Street West, Hamilton, ON, L8S4K1, Canada

⁴Department of Astrophysics, American Museum of Natural History, 200 Central Park West, New York, NY 10024, USA

⁵Department of Astrophysics, Türkenschanzstraße 17 (Sternwarte), 1180 Wien, Austria

⁶Universidad Nacional Autónoma de México, Instituto de Radioastronomía y Astrofísica, Antigua Carretera a Pátzcuaro 8701, Ex-Hda. San José de la Huerta, 58089, Morelia, Michoacán, México

⁷Universität Heidelberg, Zentrum für Astronomie, Institut für Theoretische Astrophysik, Albert-Ueberle-Str. 2, 69120 Heidelberg, Germany

⁸Universität Heidelberg, Interdisziplinäres Zentrum für Wissenschaftliches Rechnen, Im Neuenheimer Feld 225, 69120 Heidelberg, Germany

Version March 10, 2026

Abstract

The relationship between magnetic field strength and gas density is essential to understand the interstellar medium and star formation. Zeeman measurements in dense atomic and molecular gas phases have traditionally been used to directly probe magnetic field strengths in the Milky Way. This allowed derivation of a relationship between magnetic field strength B and gas number density n . We recently generalized this relation as a two-part power-law with non-zero slopes and a transition density given as $B/B_0 \propto (n/n_0)^{\alpha_1}$ for $n \leq n_0$ and $(n/n_0)^{\alpha_2}$ for $n > n_0$. Here, we extend our previous hierarchical Bayesian framework by incorporating a large body of pulsar observations that probe the diffuse interstellar medium and explicitly modelling density uncertainties through a global log-density correction parameter R applied to all densities. We also account for magnetic field geometry and measurement uncertainties through a magnetic hyperparameter to estimate B . This results in a stronger constraint on the diffuse gas part of the B - n relation. Our results confirm a non-zero exponent in the diffuse gas and a broad transition density with our best model and data set yielding maximum a posteriori results of $\alpha_1 = 0.18_{-0.02}^{+0.02}$, $\alpha_2 = 0.63_{-0.05}^{+0.08}$, $n_0 = 1630_{-1430}^{+2560} \text{ cm}^{-3}$, and $B_0 = 7.60_{-3.47}^{+2.00} \mu\text{G}$.

1. INTRODUCTION

Magnetic fields are a dynamically important component of the interstellar media (ISM) of galaxies, affecting processes as diverse as cosmic ray propagation, pressure support in diffuse gas, and star formation in the denser phases. In the latter case, although the details remain uncertain (see for example Hennebelle & Inutsuka 2019; Pattle et al. 2023) theoretical and computational work suggest that magnetic fields can support molecular clouds and filaments against large scale collapse, reducing star formation rates (Mestel & Spitzer 1956; Nakano 1973; Mouschovias 1976; Fiege & Pudritz 2000; Robinson & Wadsley 2024; Pillsworth et al. 2025; Bogue et al. 2026). The density at which the dynamical impact of magnetic fields changes may also be particularly important during the transition from warm to cold, star-forming gas (McGuinness et al. 2026). This, in turn, can affect the life cycle of giant molecular clouds, potentially changing how much molecular gas forms from the more diffuse ISM (Whitworth et al. 2023). Understanding this transition from diffuse to dense gas and where it occurs in the ISM is key to our understanding of molecular cloud formation and evolution, which in turn is important for explaining star formation and

galaxy evolution.

Given that physical processes in the diffuse ISM differ from those in the molecular, self-gravitating gas in which stars form, it is natural to investigate a two-part broken power law relation between magnetic field strength and gas density in the diffuse vs. denser gas. This gives rise to a general B - n relation of the form (Crutcher et al. 2010, hereafter C10, Jiang et al. 2020, Whitworth et al. 2025, hereafter Paper I)

$$|\mathbf{B}| = B_0 \begin{cases} (n/n_0)^{\alpha_1} & \text{if } n \leq n_0, \\ (n/n_0)^{\alpha_2} & \text{if } n > n_0, \end{cases} \quad (1)$$

where B_0 and n_0 are the normalisation parameters, and α_1 , α_2 are the power-law indices on either side of the break density, n_0 . The value of the critical density n_0 characterizing the transition between these two regimes depends upon the power law indices. Thus, the first Bayesian analysis of the Zeeman data by C10 (also see Jiang et al. 2020) gives critical densities of $\sim 300 \text{ cm}^{-3}$, while assuming that $\alpha_1 = 0$. In more recent work, no restrictive assumptions are made about the power-law indices (Paper I), resulting in a larger range of critical densities; $4000_{-3000}^{+13000} \text{ cm}^{-3}$ and $\alpha_1 = 0.15_{-0.09}^{+0.06}$.

The results of this latter, more general Bayesian analysis are in agreement with MHD simulations of dwarf galaxies (Whitworth et al. 2025; McGuinness et al. 2026). McGuinness et al. (2026) showed that the field is dominant across the warm to cold phase transition regime of $1 < n \lesssim 1000 \text{ cm}^{-3}$.

Different tracers of the magnetic field probe distinct phases of the ISM. Thus, assembling a unified B - n relation across the entire ISM remains a challenge (Beck 2015; Ferrière 2020; Seta & Federrath 2022; Gent et al. 2023). As an example, polarized dust emission traces dense molecular gas through the Davis-Chandrasekhar-Fermi (DCF) method, Zeeman measurements typically target mid- to high-column density regions, while pulsar rotation measures probe the more diffuse, ionized medium. Each of these probes different components or projections of the magnetic field: line-of-sight (LOS) for Zeeman and rotation measure and plane-of-sky for DCF measurements. Paper I showed that a two-part power-law arises when including DCF measurements. However, care must be taken when comparing these data because different magnetic field geometries are being probed between Zeeman-splitting (LOS) and DCF (plane-of-sky) measurements. Furthermore, the DCF fit appears elevated relative to Zeeman data due to known systematic overpredictions in DCF by factors of ~ 4 – 6 arising from line-of-sight averaging and turbulence assumptions (see e.g., Chen et al. 2022; Pattle et al. 2023). This paper focuses exclusively on LOS B measurements (Zeeman and pulsars) to maintain geometric consistency.

There are at least two major considerations in constraining the observationally derived B - n relationship. The first is to secure broad and deep observational data sets. The diffuse ISM and molecular gas taken together cover many decades in density over which accurate measurement of field strengths is, at the very least, challenging. Although the observational data used in Paper I covered a wide range of density and field strengths, it still lacked measurements of magnetic fields at very low densities in the diffuse gas. In this paper, we update our analysis by including in our sample values of the average LOS B for over 200 pulsars in the diffuse ISM (Seta & McClure-Griffiths 2025).

The second consideration is that both variables have substantial measurement uncertainties. The volume number density n cannot be measured directly, so it must be inferred from variables such as temperature, column density, and model-dependent assumptions about cloud geometry and excitation conditions (Pineda et al. 2010; Leroy et al. 2017). The new pulsar-based LOS B estimates, derived from rotation and dispersion measures (e.g. Seta & McClure-Griffiths 2025; Dhakal & Seta 2025), are similarly sensitive to LOS integration effects. In contrast, Zeeman splitting estimates (e.g. Heiles & Crutcher 2005; Crutcher 2012) provide more localized constraints but are susceptible to measurement noise and LOS ambiguity (C10). Therefore, accurate inferences about the B - n scaling require careful propagation of uncertainties in both quantities. In this paper, we provide a more sophisticated treatment of the errors than in Paper I by running a more general Bayesian hierarchical treatment using an extended set of hyperparameters.

To illustrate the importance of obtaining better and more extensive measurements and error estimates in

modelling the B - n relationship, we note that a different kind of scaling has been derived using the pulsar data. It is based upon the comparison of turbulent kinetic and magnetic energy densities (Seta & McClure-Griffiths 2025). The advantage of this model is that it overcomes the necessity of reconstructing the volumetric density, as the errors in turbulent velocities strongly outweigh the errors in number density. The result is a single, linear magnetic to turbulent kinetic energy density relation. However, this does not help our understanding of the transition between diffuse ISM and dense molecular clouds, and it becomes difficult to isolate the role that the magnetic field plays here.

In this paper, we build upon Paper I by including LOS magnetic field measurements deduced from pulsar data from Seta & McClure-Griffiths (2025), which includes densities at least two orders of magnitude lower than in C10, reaching $n < 10^{-2} \text{ cm}^{-3}$. Also, we implement a more general hierarchical Bayesian analysis of the errors by exploring four models with more extensive parameter sets than used in our previous paper. In Section 2, we introduce the new extended data set and our four models. Section 3 shows the results from these extended models and data sets. Section 4 discusses the results and how the different approaches affect the relationship. Finally, Section 5 summarises our key findings.

2. METHODS

2.1. Previous treatments of errors

C10 used reported errors on B . They described the uncertainty in the observed density value n_{obs} as a fixed error of a factor of two. Tritsis et al. (2015) and Jiang et al. (2020) reanalysed the data using different approaches and showed that this estimate of a factor of two is likely too low. Tritsis et al. (2015) used a more relaxed assumption and a least squares fit approach, while Jiang et al. (2020) used a Bayesian approach and allowed the error in n to be a free parameter. Jiang et al. (2020) report possible values of the fractional uncertainty on n , ranging over 7.7 – 44.1, with 9.3 being the most likely. Paper I also reanalysed the data using three different values for the fractional uncertainty, 2, 5, and 9, reporting their best result with a value of 5. However, this approach assumes that each data point has the same error factor, which is highly unlikely due to the different environments, telescopes, and projection effects at play. In Section 2.3 we present a new global parameter for n that aims to account for these effects.

There have been more recent Zeeman surveys of magnetic field strengths than those reported in C10, but of these, only Hwang et al. (2024) report estimates on the number density n , with the rest only providing column densities (Thompson et al. 2019; Nakamura et al. 2019; Koley et al. 2021; Ching et al. 2022). Inferring three-dimensional densities from two-dimensional, LOS observations is challenging, as it requires an independent input regarding the path length. Accurate estimates of n require reliable knowledge of both the geometry and morphology of the cloud, as well as precise distance measurements (Crutcher 2012). While the combination of line emission observations with reconstructed three-dimensional dust mapping (Edenhofer et al. 2024) can help identify the LOS distribution of the gas (see, for

example, Zucker et al. 2021; Angarita et al. 2024; Soler et al. 2025), it demands high-resolution density reconstructions both along the LOS and across the plane of the sky (with three-dimensional dust maps matching the angular resolution and pixel scales of the line emission data), plus prior assumptions about cloud and filament shapes.

2.2. Extended data sets: pulsars

In Paper I, we used the original 137 Zeeman data points from C10, which targeted cold neutral H I with $10 \lesssim n \lesssim 300 \text{ cm}^{-3}$ as well as higher-density OH and CN measurements in molecular clouds. In this paper, we further include the additional six Zeeman measurements from Hwang et al. (2024). We exclude DCF data here due to its plane-of-sky geometry and factor of ~ 6 overprediction relative to LOS methods (e.g. Pattle et al. 2023), which complicates joint Bayesian modelling without custom likelihood adjustments for these systematics; our LOS-only focus enables robust extension to pulsars probing low-density gas (Seta & McClure-Griffiths 2025).

The pulsar measurements from Seta & McClure-Griffiths (2025) include a total of 212 points that probe down to densities of $\sim 10^{-2} \text{ cm}^{-3}$. This is critically important because these low density points provide considerable leverage on the diffuse part of the B - n relation not otherwise obtainable. These observations derive average electron density from the ratio of the dispersion measure to pulsar distance, and the line-of-sight component of the magnetic field from the ratio between the rotation and dispersion measures, assuming uncorrelated thermal electron density and magnetic fields along the line of sight (Seta & Federrath 2021). These methods have long been used to study Galactic magnetic fields in low-density gas (Hewish et al. 1968; Smith 1968; Manchester 1974; Han 2017)

In combination, these data expand the number density range to $10^{-2} \text{ cm}^{-3} < n < 10^7 \text{ cm}^{-3}$, as well as increase the number of data points from 137 to 355. In Figure 1 we show the entire extended data set. One point circled in the Zeeman data lies above the bulk of the data and the original relation in C10.¹ The inclusion of the pulsar measurements markedly strengthens our analysis, providing leverage on both the inferred diffuse slope α_1 and the characteristic density n_0 , as we shall demonstrate.

We ran our analysis on the full data set as well as after removing the outlier to test how impactful it is. Therefore, our study includes four Data Sets (DS):

- DS1: Original Zeeman data (C10)
- DS2: Original Zeeman data with outlier removed
- DS3: Expanded Zeeman (C10; Hwang et al. 2024) and pulsar data (Seta & McClure-Griffiths 2025)
- DS4: Expanded Zeeman and pulsar data with outlier removed

¹ C10 note that this point corresponds to the giant molecular cloud Sgr B2 North, suggesting it likely has significant errors on n . This interpretation is supported by Jiang et al. (2020), whose Bayesian Model C, using a framework similar to C10, showed little variation under the assumption of this outlier. However, when they modified the Bayesian setup, the outlier became more significant.

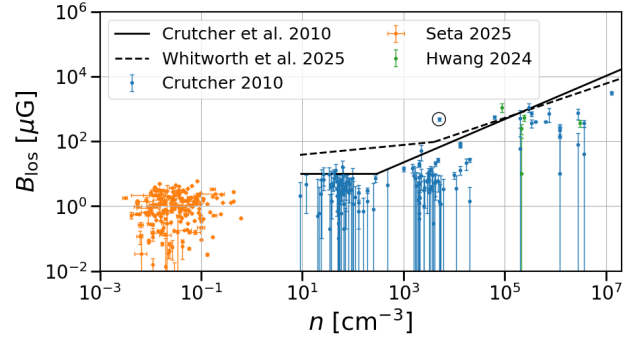


FIG. 1.— Full data set including Zeeman data from C10 and Hwang et al. (2024) and pulsar data from Seta & McClure-Griffiths (2025). Lines show C10 upper-limit power law (solid line) and the Paper I MAP result (dashed line), which, as discussed in Appendix A, had too high a value of B_0 . (Note that Fig. 1 of Seta & McClure-Griffiths 2025 used the preliminary result from an early preprint version of Paper I.) The outlier in the Zeeman data is circled for identification, see main text for further details (C10).

By including more measurements in the diffuse gas and applying a new hierarchical Bayesian approach we aim to constrain the diffuse slope in the relationship and probe the break transition in more detail.

2.3. Extended Hierarchical Bayesian Model

We extend our hierarchical models (Paper I) by incorporating several modifications inspired by Jiang et al. (2020). Because both the Zeeman and pulsar measurements provide LOS-averaged magnetic field strengths that, owing to projection and cancellation effects, represent lower limits to the true field strength, a hierarchical model accounting for these effects and allowing for statistical inference on the upper field envelope is required.

In all our models, we retain the same piecewise power-law envelope for the magnetic field introduced in Paper I and given by Equation (1), a log-space treatment of priors and parameter space, and Gaussian likelihood in $\log B$. We implement a *global* multiplicative correction factor R , such that the corrected log densities are calculated from a hyperparameter f_n , which represents the linear-space fractional correction to the reported density $n_{\text{model},i} = (1 + f_n)n_{\text{obs},i}$. From this we define the global log-space density correction:

$$R \equiv \log_{10}(1 + f_n). \quad (2)$$

such that the corrected densities in log space are

$$\log_{10} n_{\text{model},i} = \log_{10} n_{\text{obs},i} + R, \quad (3)$$

This applies the same systematic correction factor to all sources.

This differs from previous approaches in that we do not require per-source error estimates, and is physically motivated because the primary sources of uncertainty in n , for example assumptions about path length, excitation conditions, and line-of-sight averaging, affect all sight lines. Applying a global factor therefore provides a reasonable first-order correction that captures the average systematic bias while remaining tractable within the hierarchical Bayesian framework.

The envelope-scaling hyperparameter f_B captures the effects of projection and LOS systematics, analogous in

role to the f parameter(s) in Jiang et al. (2020). However, we assign f_B log-normal rather than uniform priors, which better captures the expected scatter in projection effects. We therefore define the transform in log space as:

$$\log_{10} B_{\text{obs}} = \log_{10} B_{\text{model}} + \log_{10} f_B \quad (4)$$

This parameter statistically adjusts the predicted magnetic field strength to account for systematics that reduce observed field strengths relative to true values. This allows the model to represent the upper envelope of true values statistically without having to construct it explicitly.

Finally, to capture additional field dispersion, we introduce a free parameter σ_B controlling the intrinsic scatter in $\log_{10} B$, due to line-of-sight averaging through turbulent fields and variation across different regions beyond that captured by the measurement errors.

We define $\log_{10} B_{\text{model},i}$ as the deterministic, noise-free magnetic field predicted by the broken power-law envelope at the corrected density $n_{\text{model},i}$. That is, $\log_{10} B_{\text{model},i}$ is given by Eq. (5) for each observation i . We can therefore interpret $B_{\text{model},i}$ as the upper-envelope relation in a statistical sense.

$$\log_{10} B_{\text{model},i} = \log_{10} B_0 + \begin{cases} \alpha_1 (\log_{10} n_{\text{model},i} - \log_{10} n_0) & \text{if } \log_{10} n_{\text{model},i} \leq \log_{10} n_0, \\ \alpha_2 (\log_{10} n_{\text{model},i} - \log_{10} n_0) & \text{if } \log_{10} n_{\text{model},i} > \log_{10} n_0. \end{cases}$$

We model the total scatter $\sigma_{B,i,\text{total}}$ in a magnetic field observation B_i as a combination of intrinsic and measured components,

$$\sigma_{B,i,\text{total}}^2 = \sigma_B^2 + \sigma_{B,i}^2, \quad (6)$$

where $\sigma_{B,i}$ is the per-source observational uncertainty of the measured field in log space, σ_B is the intrinsic scatter inferred as a hyperparameter, and i is the observation.

The log-likelihood for the observed log-field values $\log_{10} B_{\text{obs},i}$ and set of hyperparameters θ is:

$$\ln p(B_{\text{obs},i} | \theta) = -\frac{1}{2} \sum_{i=1}^n \left[\left(\frac{\log_{10} B_{\text{obs},i} - (\log_{10} B_{\text{model},i} + \log_{10} f_B)}{\sigma_{B,i,\text{total}}} \right)^2 + \ln \sigma_{B,i,\text{total}}^2 \right] + \text{const}, \quad (7)$$

where $(B_{\text{model},i}(\theta))$ is the deterministic envelope prediction from Equation (5). This log-likelihood function, allows the observed values to lie below this curve due to the envelope scaling factor f_B along with additional intrinsic scatter.

The log-likelihood assumes that the observed magnetic field $B_{\text{obs},i}$ is drawn from a normal distribution centred on the predicted value $\log_{10} B_{\text{model},i}(\theta)$, with total variance $\sigma_{B,i}^2$ accounting for both intrinsic scatter and measurement uncertainty. Thus, the agreement between each measured $\log_{10} B_i$ and predicted $\log_{10} B_{\text{model},i}$ from the corrected density $\log_{10} n_{\text{model},i}$ is rigorously assessed.

We implement the models in a fully vectorized log-likelihood evaluation for computational efficiency.

Below we highlight the aspects that differ between models. The full set of model hyperparameters and priors for each model are given in Table 1.

2.3.1. Model A - Free density correction

This is our fiducial model, described above.

2.3.2. Model B - Fixed density correction

Our second model has one key difference to the fiducial model: we use a linear multiplicative factor for the density correction in order to easily compare to previous work on this topic. Specifically, we define:

$$\log_{10} n_{\text{model},i} = \log_{10} n_{\text{obs},i} + \log_{10}(1 + f_n), \quad (8)$$

where $(1 + f_n)$ represents the linear correction factor. We test values of $(1 + f_n) = 2, 5,$ and 9 , corresponding to log-space corrections of $R = 0.30, 0.70,$ and 0.95 . These values are motivated by the density uncertainties used by C10, Paper I, and Jiang et al. (2020), respectively, though those works used per-source scatter rather than a global correction. While those works applied per-source corrections, our implementation provides a global multiplicative factor, bridging our log-density method with the earlier per-source approaches.

2.3.3. Model C - Two-envelope model with flexible density correction

(5) Having tested the new approach with Models A and B, we next improve upon them by taking Model A and generalising the single magnetic field envelope-scaling parameter f_B into two parameters, $f_{B,1}$ and $f_{B,2}$, applied respectively below and above n_0 . This is motivated by the expectation that the magnetic field in diffuse gas behaves differently from that in dense gas (Jiang et al. 2020, Paper I) due to different density and turbulent velocity properties (Seta & McClure-Griffiths 2025), and by the possibility that projection effects, field tangling, and/or beam averaging differ systematically between these regimes due to different size and morphology of structures. Both $f_{B,1}$ and $f_{B,2}$ are treated as global hyperparameters and inferred simultaneously from the data, allowing for different envelope realisations above and below the break density.

To obtain a well-behaved Bayesian model and ensure convergence, we slightly modify our priors and bounds relative to Models A and B. The additional levels of complexity in this model increase parameter degeneracies, and overly wide priors can therefore prevent the sampling routine from converging. This results in having to adopt narrower priors informed by the posterior constraints from Models A and B.

2.3.4. Model D - Two-envelope model with reported pulsar density errors

Model D uses the same hyperparameter set as Model C but modifies the treatment of density errors for the pulsar data by incorporating the reported density errors. Unlike the Zeeman measurements, the pulsar density estimates can include error estimates via the propagation of dispersion measure uncertainties as well as distance

uncertainties when available (out of 212 pulsars, distance uncertainties are available for 126 pulsars only; see [Manchester et al. 2005](#)). By including these reported errors, the Bayesian framework can more realistically account for measurement limitations in pulsar-derived densities. However, because these errors are relatively small compared to the systematic uncertainties, we retain the global log-density correctional parameter R , which both contributes to the effective systematic shift alongside reported uncertainties and supplies an effective error floor.

For each data point i we modify Equation 3:

$$\log_{10} n_{\text{model},i} = \log_{10} n_{\text{obs},i} + n_{\text{eff},i}, \quad (9)$$

where the effective error, $n_{\text{eff},i}$ combines the fractional and reported contributions in quadrature:

$$n_{\text{eff},i} = \sqrt{R^2 + (\log_{10} \sigma_{n,i})^2}, \quad (10)$$

and $\sigma_{n,i}$ is the reported fractional error on n for each pulsar measurement. For the pulsar data, we use the reported values of $n_{\text{err},i}$; for the Zeeman data, we set $n_{\text{err},i} = 0$, so that the total uncertainty there is then governed entirely by f_n . As in the previous models, we report R as given by Equation (2).

In this model, f_n contributes as an effective systematic shift that combines with the reported measurement errors in quadrature, providing a minimum correction when no errors are reported (as in Models A and C). Allowing for two envelope parameters and the additional error propagation increases the flexibility of the model but also amplifies parameter degeneracies. We therefore adopt the same limits and priors as in Model C. As this only affects the pulsar data sets, we only run the model on DS3 and DS4.

2.4. Posterior Sampling and Chains

We use a Hamiltonian Monte Carlo (HMC) approach to sample posteriors. As an improvement of the traditional Metropolis-Hastings Markov Chain Monte Carlo (MCMC [Metropolis et al. 1953](#)) approach, the HMC algorithm uses gradient information to take informed steps, reducing random-walk behaviour and therefore requiring fewer samples to reach convergence ([Neal 2011](#); [Betancourt 2017](#)). We use the HMC algorithm due to its ability to explore efficiently high-dimensional parameter spaces.

Posterior samples are generated using HMC ([Neal 2011](#)), as implemented in `Stan`, a statistical modelling language² accessed from a Python wrapper, specifically version 1.2.5 of the package `CmdStanPy`³. In particular, we use the No-U-Turn Sampler with parameters `adapt_delta = 0.99` and `max_treedepth = 15` tuned to optimize acceptance rate and mixing.

In all models, we use four independent chains, which is a commonly adopted standard for MCMC sampling. It allows for robust convergence diagnostics while balancing computational cost and efficiency. Each chain is initialised from pseudo-random initial values to robustly explore the parameter space. Each chain consists of 5 000 warm-up iterations followed by 5 000 sampling iterations.

Chain convergence is assessed using the potential scale reduction factor \hat{R} ([Gelman & Rubin 1992](#)) and the effective

sample sizes for bulk and tail posterior distributions, both computed automatically by the HMC implementation. Note that \hat{R} is distinct from the fractional uncertainty parameter R ; it diagnoses and convergence by comparing between and within-chain variability across independent MCMC chains. For an \hat{R} close to unity, all chains are considered to have mixed well and converged to the stationary posterior distribution. Whilst convergence is typically achieved quickly, our choice of number of sampling iterations per chain ensures a large sample size across all parameters, minimises variability due to random initialisations, and ensures thorough mixing. Posterior samples are then used to construct credible intervals, medians, maximum-a-posteriori (MAP) estimates, and corner plots for each model and dataset.

3. RESULTS

In this section we present the results of our extended hierarchical Bayesian approach that includes the original and extended data sets. We focus on the MAP results as these represent the parameter values at the peak of the posterior distribution (i.e., something like a best fit in a Bayesian sense).

3.1. Model A - Free density correction

Figure 2 and Table 2 show the results for the inferred MAP results for each dataset, with the 68% highest posterior density (HPD).

Across all data sets, the MAP for α_1 is well constrained, with $\leq 10\%$ variation, with small errors, from $0.18_{-0.03}^{+0.02}$ to $0.20_{-0.20}^{+0.03}$. The value for α_2 is dependent on whether the outlier is included or not, rising from 0.63 to 0.68 when it is removed, in line with [Jiang et al. \(2020\)](#). We note that this shift is within the 68% HPD, though only just, and that it is larger than the $\sim 10\%$ variation seen in α_1 .

The break density, n_0 , is somewhat uncertain and variable between datasets, ranging from $1.51_{-1.51}^{+0.71} \times 10^3 \text{ cm}^{-3}$ to $5.71_{-5.30}^{+0.89} \times 10^3 \text{ cm}^{-3}$. Our inferred values are about an order of magnitude larger than originally reported in [C10](#) of 300 cm^{-3} , but compatible with [Paper I](#). The extended data sets DS3 and DS4, when the outlier is removed, show a smaller increase, $\sim 1000 \text{ cm}^{-3}$, compared to the Zeeman only data, $\sim 2100 \text{ cm}^{-3}$. Again we note that these are within the 68% HPD, but also note that here the lower limit can be as large as 100% of the MAP value with upper limits being up to 50% of the MAP.

The inclusion of the pulsar data leads to a slightly larger inferred value of B_0 , ranging from $14.41_{-13.39}^{+11.19} \mu\text{G}$ to $58.53_{-54.10}^{+18.13} \mu\text{G}$, compared to the original result of $10 \mu\text{G}$ in [C10](#). In both the Zeeman-only and the extended Zeeman plus pulsar data, B_0 increases when the outlier is removed.⁴

The estimated global log-density correction R , which quantifies the systematic bias in the underlying density measurements, is found to be consistent at around 1 for the Zeeman-only datasets DS1 and DS2, both with and without the outlier. Although the uncertainty on R spans

⁴ Compared to the result in [Paper I](#), $B_0 = 61.00_{-14.00}^{+63.00} \mu\text{G}$, these seem reasonable. However, whilst developing the new code an error in the original code was found that led to an overprediction of B_0 . See [Appendix A](#) for a discussion on this.

² <https://mc-stan.org/>

³ <https://mc-stan.org/cmdstanpy/>

TABLE 1
MODEL HYPERPARAMETERS AND PRIORS

Parameter		A	Model B	C/D
B_0	Envelope normalization (μG)	$\log_{10} B_0 \sim \mathcal{N}(0, 2)$ $> -10 - Y_{\min}$	as A	as A
n_0	Break density (cm^{-3})	$\log_{10} n_0 \sim \mathcal{N}(0, 2)$ $> -10 - X_{\min}$	as A	as A
α_1	Low- n slope	$\mathcal{N}(0.5, 0.5)$ > 0	as A	$\mathcal{N}(0.2, 0.2)$ [0, 1]
α_2	High- n slope	$\mathcal{N}(0.5, 0.5)$ > 0	as A	$\mathcal{N}(0.6, 0.2)$ [0, 1]
f_B	Envelope scaling	$\log_{10} f_B \sim \mathcal{N}(0, 1.0)$ [$10^{-4}, 1$]	as A	–
$f_{B,1}$	Low- n envelope scaling	–	–	$\log_{10} f_{B,1} \sim \mathcal{N}(0, 0.1)$ [$10^{-4}, 1$]
$f_{B,2}$	High- n envelope scaling	–	–	$\log_{10} f_{B,2} \sim \mathcal{N}(0, 0.1)$ [$10^{-4}, 1$]
σ_B	B scatter (\log_{10})	$\mathcal{N}(0, 1.0)$ > 0	as A	$\mathcal{N}(0.1, 0.1)$ [0, 10]
f_n	Global density correction reported as $R = \log_{10}(1 + f_n)$	$\log_{10} f_n \sim \mathcal{N}(0, 1.0)$ [-2, 3]	$(f_n + 1)$ fixed as: 2, 5, 9	as A

Notes. The top line for each parameter shows the prior choice whilst the bottom shows the HMC bounds. Model B fixes R to literature values. C/D use dual $f_{B,1}$, $f_{B,2}$.

a wide range (~ 0.32 to 1.1 for DS2), the central values are in line with those used in earlier studies such as (Jiang et al. 2020). In the extended datasets DS3 and DS4, the value is consistent at ~ 0.45 with similar uncertainties. This suggests that only a small amount of correction bias in n is needed by the model to account for the observed data.

The intrinsic scatter in magnetic field strength, σ_B , is similarly small and consistent in the extended dataset, within uncertainties. In the Zeeman-only datasets DS1 and DS2, there is a slight decrease when the outlier is removed. The scaling envelope f_B shown in Figure 2 represents the range over which B could plausibly lie, with the MAP being the upper limit. Because f_B acts additively in log space, a smaller value means a greater downward offset from the upper envelope, and thus a larger shaded region between the upper envelope and the f_B -scaled curve. Conversely, as f_B approaches 1, $\log_{10} 1 = 0$, so the shaded region narrows. This reflects that a lower value of f_B indicates a larger reduction in observed field strength due to projection and other systematics. Table 2 shows that the Zeeman-only results DS1 and DS2 yield a smaller f_B compared to the combined datasets, while removing the outlier also reduces f_B slightly. This is understandable: with fewer data points, there is a greater apparent reduction from the upper envelope, thus the model infers a larger suppression, i.e. smaller f_B .

3.2. Model B - Fixed density correction

Table 3 presents the MAP results for Model B, while Figure 3 shows the MAP fits for each data set at each

fixed value of R (for readability, we do not plot the 100 sample lines or f_B region).

Similar to Model A, α_1 is well constrained across all data sets and values of R , with typical values of ~ 0.19 . α_2 also remains consistent, but shows some variation between datasets due to sensitivity to the outlier, similar to Model A. The break density n_0 shows a strong dependency on R . As R increases, both n_0 and its associated uncertainties increase. For all values of R , n_0 is lower in the extended datasets DS3 and DS4, showing the influence of the low-density pulsar data, even at high fractional uncertainty.

The value of B_0 shows no systematic trend across datasets and R , nor does the envelope scaling function f_B . They do not correlate with the outlier, where they both increase and decrease, or R , or whether the pulsar data is included or not. Both parameters fluctuate, which likely reflects that Model B's fixed uncertainty structure is less sensitive to these, or that the underlying data possess too much heterogeneity for consistent trends to emerge. The intrinsic scatter, σ_B , is consistent across values of R in the same manner as Model A.

3.3. Model C - Two-envelope model with flexible density correction

Table 4 presents the MAP results for Model C, while Figure 4 shows the MAP fits for each dataset, with the two envelope scaling factors $f_{B,1}$ and $f_{B,2}$ shown.

The value of α_1 exhibits greater variation in this model than in the previous two, from $0.12_{-0.12}^{+0.05}$ in DS1 to $0.19_{-0.02}^{+0.02}$ in DS4. For the Zeeman-only dataset DS1, α_1 is

TABLE 2
MAP VALUES FROM MODEL A.

Data Set	α_1	α_2	n_0 (10^3cm^{-3})	B_0 (μG)	f_B	σ_B	R
DS1	$0.20^{+0.03}_{-0.20}$	$0.63^{+0.04}_{-0.06}$	$3.66^{+0.13}_{-3.36}$	$27.69^{+11.12}_{-23.47}$	$0.31^{+0.19}_{-0.31}$	$0.31^{+0.04}_{-0.02}$	$0.97^{+0.46}_{-0.96}$
DS2	$0.20^{+0.03}_{-0.20}$	$0.68^{+0.02}_{-0.08}$	$5.71^{+0.89}_{-5.30}$	$58.53^{+18.13}_{-54.10}$	$0.17^{+0.35}_{-0.16}$	$0.26^{+0.03}_{-0.02}$	$1.11^{+0.32}_{-1.10}$
DS3	$0.18^{+0.02}_{-0.03}$	$0.63^{+0.06}_{-0.09}$	$1.51^{+0.71}_{-1.51}$	$14.41^{+11.19}_{-13.39}$	$0.42^{+0.14}_{-0.41}$	$0.44^{+0.02}_{-0.02}$	$0.45^{+0.41}_{-0.44}$
DS4	$0.18^{+0.02}_{-0.02}$	$0.68^{+0.04}_{-0.11}$	$2.45^{+1.35}_{-2.45}$	$39.90^{+7.80}_{-36.60}$	$0.17^{+0.39}_{-0.16}$	$0.42^{+0.02}_{-0.02}$	$0.46^{+0.36}_{-0.45}$

Notes. R is the inferred global log-density correction for the observed number density: it is inferred in Models A, C, and D. f_B is the multiplicative factor scaling the envelope. σ_B is the fractional uncertainty that is applied to the errors on B . DS1 is the original Zeeman data, DS2 is the Zeeman data with its outlier removed, DS3 is the Extended Zeeman data with pulsar data added, and DS4 is the Zeeman plus pulsar data with both outliers removed. The errors are the bounds of the 68th percentile confidence interval.

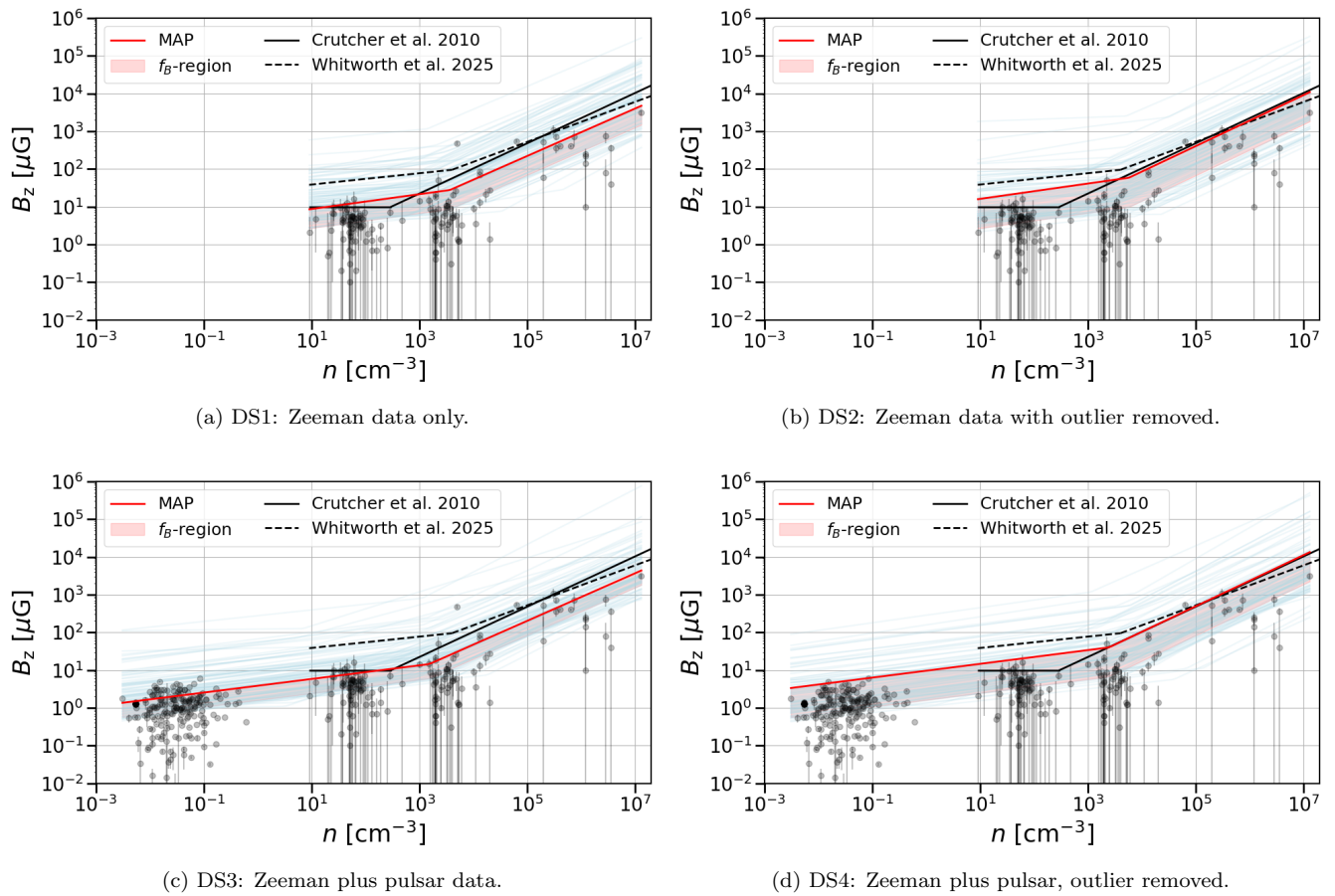


FIG. 2.— The inferred upper limit of magnetic field strength as a function of number density, based on hierarchical Bayesian analysis of Model A for each dataset (DS1–DS4: see subfigure captions). The *solid black line* in all plots is the upper envelope proposed by C10. The *red line* shows the MAP relationship between B_z and n based on our analysis, and the *blue lines* are 100 random posterior draws. The scaling envelope of f_B , shown as the *pink band*, represents how far B could plausibly lie below the MAP. The dashed line shows the result published in [Paper I](#), which had an incorrectly high value of B_0 , as is further discussed in [Appendix A](#). Error bars for n are omitted for readability.

TABLE 3
THE MAP RESULTS FOR MODEL B

Data Set	α_1	α_2	n_0 (10^3cm^{-3})	$B_0(\mu\text{G})$	f_B	σ_B	R	$(f_n + 1)$
DS1	$0.19^{+0.02}_{-0.19}$	$0.64^{+0.03}_{-0.07}$	$3.40^{+0.43}_{-2.89}$	$31.99^{+5.80}_{-28.11}$	$0.25^{+0.26}_{-0.25}$	$0.33^{+0.03}_{-0.03}$	0.30	2
DS2	$0.20^{+0.03}_{-0.20}$	$0.67^{+0.02}_{-0.07}$	$5.57^{+0.96}_{-4.81}$	$9.76^{+0.78}_{-5.57}$	$0.20^{+0.32}_{-0.20}$	$0.26^{+0.03}_{-0.03}$	0.30	2
DS3	$0.18^{+0.02}_{-0.03}$	$0.64^{+0.05}_{-0.10}$	$2.45^{+0.04}_{-2.45}$	$6.27^{+1.66}_{-2.76}$	$0.21^{+0.34}_{-0.20}$	$0.44^{+0.02}_{-0.02}$	0.30	2
DS4	$0.19^{+0.02}_{-0.02}$	$0.67^{+0.05}_{-0.09}$	$3.94^{+0.88}_{-3.51}$	$7.15^{+1.14}_{-3.11}$	$0.21^{+0.35}_{-0.20}$	$0.43^{+0.02}_{-0.02}$	0.30	2
DS1	$0.20^{+0.04}_{-0.20}$	$0.64^{+0.03}_{-0.07}$	$11.09^{+3.86}_{-9.87}$	$9.55^{+1.89}_{-5.70}$	$0.17^{+0.34}_{-0.17}$	$0.32^{+0.04}_{-0.02}$	0.70	5
DS2	$0.18^{+0.02}_{-0.18}$	$0.68^{+0.02}_{-0.07}$	$13.86^{+2.75}_{-12.04}$	$9.58^{+0.86}_{-5.44}$	$0.17^{+0.34}_{-0.17}$	$0.26^{+0.03}_{-0.02}$	0.70	5
DS3	$0.18^{+0.03}_{-0.02}$	$0.64^{+0.06}_{-0.09}$	$4.99^{+1.28}_{-4.99}$	$5.61^{+2.07}_{-2.07}$	$0.26^{+0.29}_{-0.26}$	$0.43^{+0.02}_{-0.01}$	0.70	5
DS4	$0.19^{+0.01}_{-0.03}$	$0.67^{+0.04}_{-0.10}$	$10.02^{+0.56}_{-10.02}$	$21.73^{+9.11}_{-18.05}$	$0.34^{+0.23}_{-0.33}$	$0.42^{+0.02}_{-0.01}$	0.70	5
DS1	$0.16^{+0.00}_{-0.16}$	$0.63^{+0.04}_{-0.06}$	$11.33^{+1.53}_{-9.14}$	$31.99^{+3.59}_{-28.12}$	$0.23^{+0.30}_{-0.23}$	$0.32^{+0.03}_{-0.03}$	0.95	9
DS2	$0.20^{+0.03}_{-0.20}$	$0.67^{+0.03}_{-0.07}$	$26.74^{+7.41}_{-23.58}$	$48.21^{+9.17}_{-43.85}$	$0.21^{+0.30}_{-0.21}$	$0.27^{+0.03}_{-0.03}$	0.95	9
DS3	$0.19^{+0.02}_{-0.03}$	$0.63^{+0.07}_{-0.10}$	$9.75^{+0.61}_{-9.75}$	$20.66^{+3.40}_{-19.77}$	$0.30^{+0.26}_{-0.30}$	$0.43^{+0.02}_{-0.02}$	0.95	9
DS4	$0.19^{+0.02}_{-0.03}$	$0.66^{+0.05}_{-0.09}$	$17.85^{+1.16}_{-17.84}$	$29.42^{+1.76}_{-25.81}$	$0.25^{+0.31}_{-0.24}$	$0.42^{+0.02}_{-0.01}$	0.95	9

Notes. The same headings and labels as Table 2, except for the last column, which gives the value for the linear global error correction corresponding to R in each case.

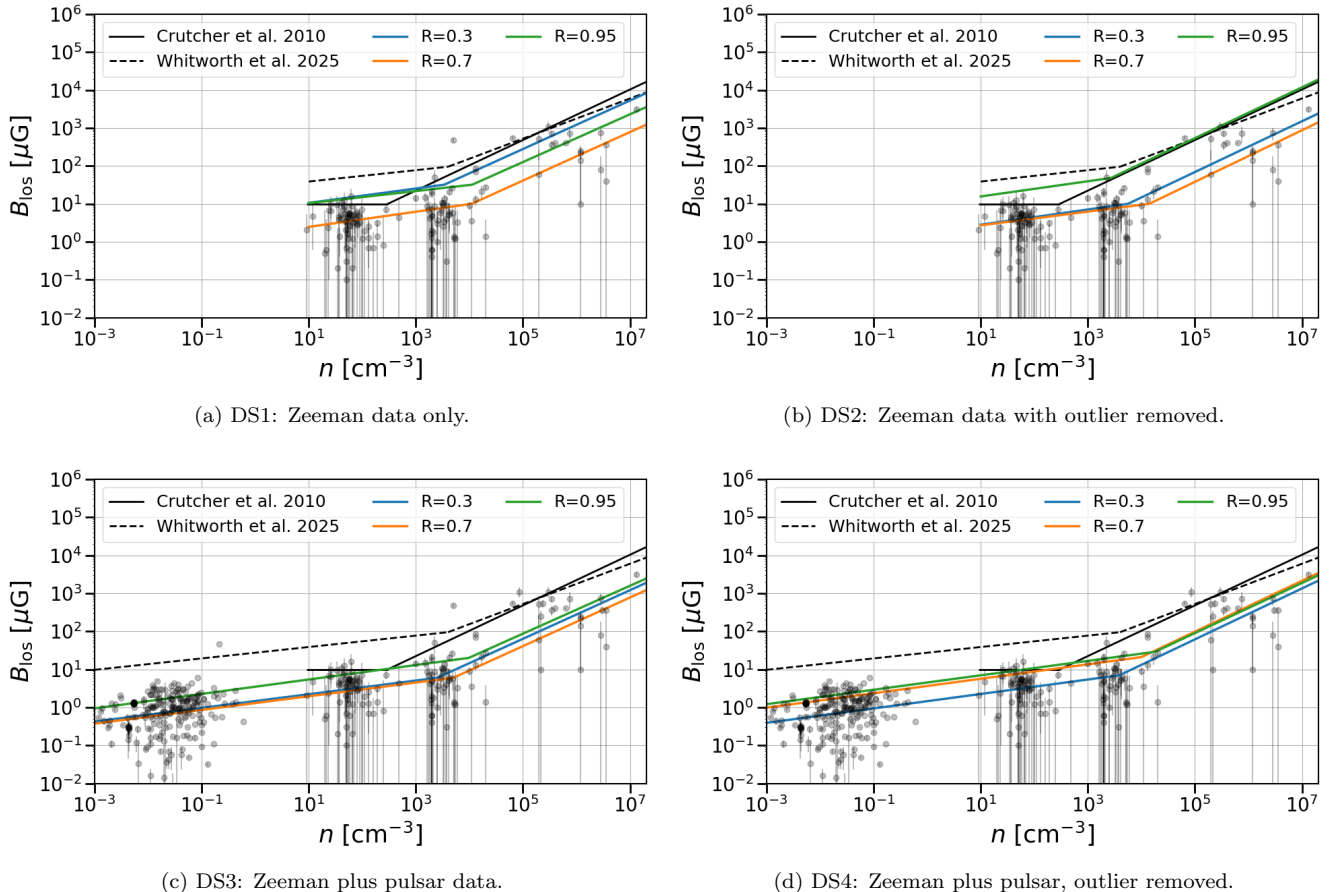


FIG. 3.— The inferred relationship of magnetic field strength as a function of number density, based on hierarchical Bayesian analysis for each dataset for Model B, with fixed linear density error parameter ($f_n + 1$). Here we plot the results for the different values of ($f_n + 1$) on the same plot for each dataset for ease of comparison between the error treatments. Otherwise the same as Fig. 2.

lower (MAP 0.12), but increases to a similar value when the outlier is excluded in DS2. There is also a large lower uncertainty for DS1 and DS2, suggesting the true value may be closer to unity. In contrast, for the extended datasets including pulsars (DS3, DS4), the uncertainties are smaller and α_1 is only marginally lower than in models A and B. Meanwhile, the maximum α_2 is only slightly lower compared to previous models at $0.66^{+0.03}_{-0.06}$, but remains well constrained by its uncertainties.

The break density n_0 follows a similar trend to models A and B, increasing when the outlier is removed, though it is lower for the Zeeman-only datasets. For the extended dataset DS3, n_0 is lower than in model A, but for DS4 it is slightly higher, indicating a stronger dependency on the outlier. The envelope normalization, B_0 , is relatively consistent between datasets, and consistent with the originally reported value of $B_0 = 10 \mu\text{G}$ in C10. However, it is much lower than Paper I where a value of $B_0 \simeq 61 \mu\text{G}$ was reported for Zeeman data.

The two envelope scaling factors $f_{B,1}$ and $f_{B,2}$, are comparable across datasets with only slight variations. This suggests the two-envelope approach is able to accommodate the observed range of magnetic field strengths across both low- and high-density regimes. The estimated global log-density correction factor R is consistent in the primary datasets (DS1 and DS2), within uncertainties, though slightly larger in the extended

datasets (DS3 and DS4). These values are slightly larger than the values used in C10 where they use a per-source factor of 2 (0.3 in log-space) which is what we return for DS1, notably the same dataset used in C10. The remaining results are similar to those reported in Jiang et al. (2020) and (Paper I). This suggests that, in this model, n requires only moderate additional correction to account for the observed data.

In contrast, σ_B , the intrinsic scatter in B , is larger here than in Model A. The use of two scaling factors appears to capture more of the observed variation in magnetic field strength as intrinsic scatter, highlighting the importance of understanding the sources and limitations of intrinsic variance in magnetic field measurements and their density or phase dependence.

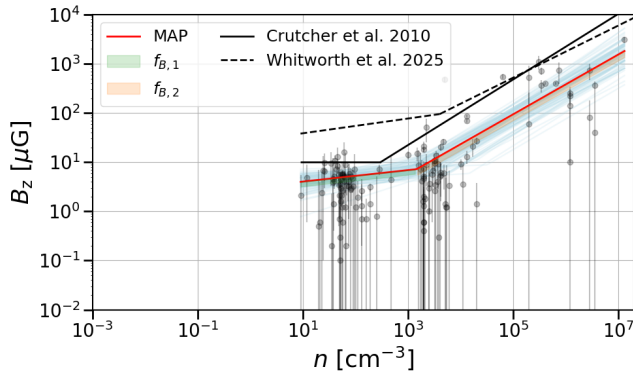
3.4. Model D - Two-envelope model with reported pulsar density errors

Table 5 presents the MAP results for Model D, which incorporates the reported errors on n for the extended datasets. Figure 5 shows the MAP fits, with the two envelope scaling factors $f_{B,1}$ and $f_{B,2}$, as in Model C.

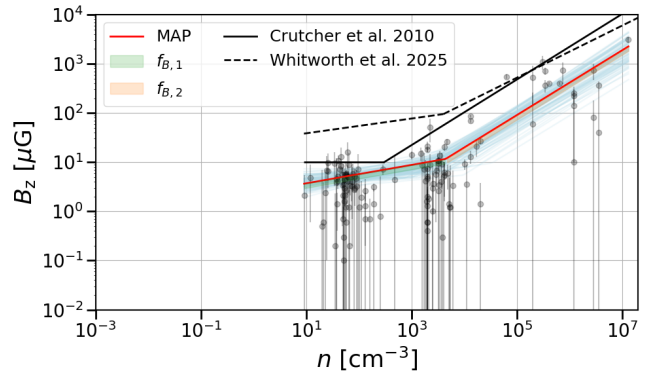
In this model, α_1 remains unchanged between the two datasets, while α_2 is the same as Model C for DS3 and only slightly smaller in DS4, with the difference lying within the uncertainties. The break density n_0 shows a smaller increase from DS3 to DS4 than in previous mod-

TABLE 4
MAP VALUES FROM MODEL C.

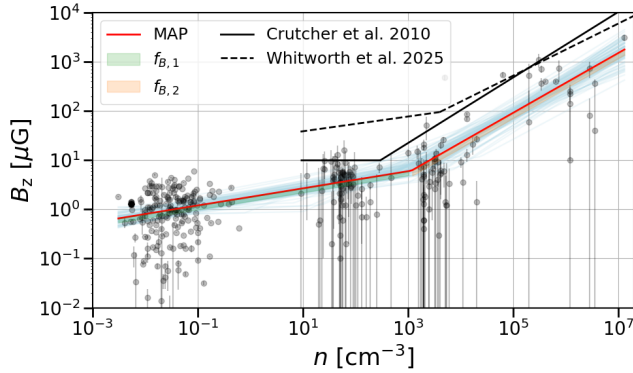
Data Set	α_1	α_2	n_0 (10^3cm^{-3})	B_0 (μG)	$f_{B,1}$	$f_{B,2}$	σ_B	R
DS1	$0.12^{+0.05}_{-0.12}$	$0.61^{+0.06}_{-0.03}$	$1.45^{+1.76}_{-1.22}$	$7.19^{+1.98}_{-2.95}$	$0.80^{+0.20}_{-0.01}$	$0.75^{+0.24}_{-0.03}$	$1.01^{+0.45}_{-0.91}$	$0.30^{+0.03}_{-0.02}$
DS2	$0.19^{+0.02}_{-0.15}$	$0.66^{+0.03}_{-0.06}$	$4.40^{+0.65}_{-4.00}$	$11.61^{+0.70}_{-7.02}$	$0.81^{+0.19}_{-0.00}$	$0.80^{+0.20}_{-0.01}$	$0.84^{+0.62}_{-0.74}$	$0.26^{+0.02}_{-0.03}$
DS3	$0.17^{+0.03}_{-0.02}$	$0.61^{+0.07}_{-0.06}$	$1.16^{+1.15}_{-1.16}$	$6.11^{+2.54}_{-2.41}$	$0.82^{+0.18}_{-0.01}$	$0.78^{+0.21}_{-0.02}$	$0.96^{+0.23}_{-0.86}$	$0.42^{+0.03}_{-0.01}$
DS4	$0.19^{+0.02}_{-0.02}$	$0.64^{+0.06}_{-0.07}$	$2.66^{+1.23}_{-2.66}$	$8.66^{+0.76}_{-4.41}$	$0.79^{+0.21}_{-0.03}$	$0.79^{+0.21}_{-0.02}$	$0.79^{+0.38}_{-0.69}$	$0.42^{+0.02}_{-0.02}$



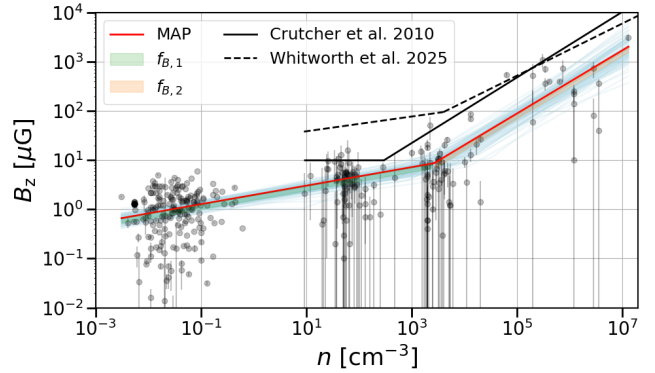
(a) DS1: Zeeman data only.



(b) DS2: Zeeman data with outlier removed.



(c) DS3: Zeeman plus pulsar data.



(d) DS4: Zeeman plus pulsar, outlier removed.

FIG. 4.— MAP results for model C with separate values of f_B above and below n_0 . The error ranges for $f_{B,1}$ (green) and $f_{B,2}$ (orange) are shown. Otherwise the same as Fig. 2.

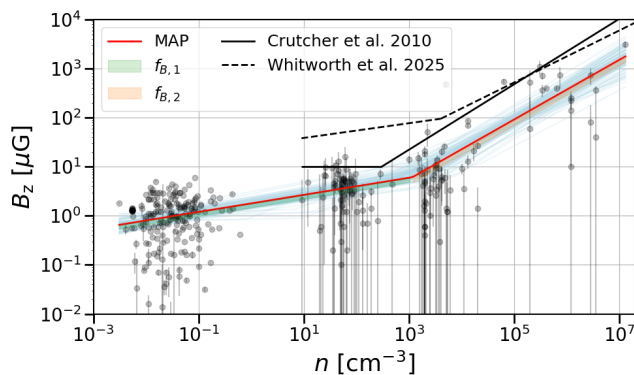
els, only a factor of ~ 1.44 , and lies within the uncertainties. We also find that B_0 lies within the uncertainties but below the original value of $10 \mu\text{G}$ in C10 with DS3 having $B_0 = 6.50^{+1.89}_{-2.80}$ and DS4 $B_0 = 7.60^{+2.00}_{-3.37}$.

The two envelope scaling factors $f_{B,1}$ and $f_{B,2}$ are comparable in the two datasets with a small decrease from the diffuse gas to the dense gas, as in Model C. This suggests the two-envelope approach is robust, though the fit

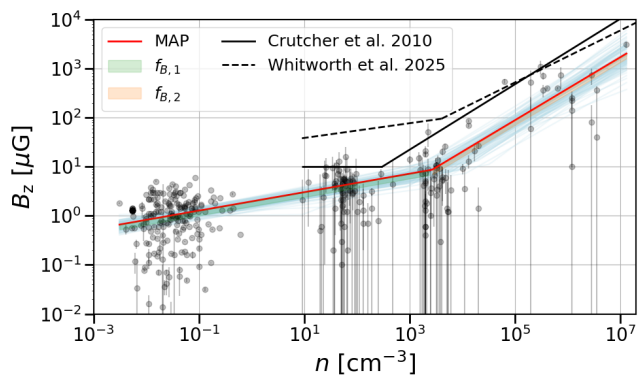
for dense gas is slightly less so, likely a consequence of there being fewer data points above n_0 . As in Model C, the estimated global log-density correction parameter R is similar to previously reported in C10 and Paper I. The intrinsic scatter parameter σ_B does show some variation. Both datasets have a smaller value of the parameter than Model C, and it becomes smaller still when the outlier is removed.

TABLE 5
MAP VALUES FROM MODEL D

Data Set	α_1	α_2	n_0 (10^3cm^{-3})	B_0 (μG)	$f_{B,1}$	$f_{B,2}$	σ_B	R
DS3	$0.18^{+0.03}_{-0.02}$	$0.61^{+0.07}_{-0.05}$	$1.13^{+1.25}_{-1.13}$	$6.50^{+1.89}_{-2.80}$	$0.83^{+0.17}_{-0.01}$	$0.78^{+0.20}_{-0.03}$	$0.80^{+0.35}_{-0.70}$	$0.43^{+0.01}_{-0.02}$
DS4	$0.18^{+0.02}_{-0.02}$	$0.63^{+0.08}_{-0.05}$	$1.63^{+2.56}_{-1.46}$	$7.60^{+2.00}_{-3.37}$	$0.80^{+0.20}_{-0.02}$	$0.75^{+0.23}_{-0.00}$	$0.55^{+0.59}_{-0.45}$	$0.41^{+0.02}_{-0.01}$



(a) DS3: Zeeman plus pulsar data.



(b) DS4: Zeeman plus pulsar, outlier removed.

FIG. 5.— MAP results for model D, including explicit pulsar density errors where available. All notations are the same as Fig. 4.

4. DISCUSSION

4.1. Model Uncertainties

We have shown that switching from a single envelope scaling parameter f_B across the full data, to using two, $f_{B,1}$ and $f_{B,2}$ on either side of the break density n_0 , and including an intrinsic scatter term σ_B , enables the models to achieve much tighter posterior constraints. By allowing $f_{B,1}$ and $f_{B,2}$ to independently scale the upper envelope in the low- and high-density regimes, the model can more flexibly accommodate variations in magnetic field strength across different environments. The inclusion of σ_B acknowledges that the reported observational uncertainties may underestimate the true scatter in B . As a result, the model does not rely solely on formal measurement errors, but also models intrinsic astrophysical variation, yielding MAP estimates that are less likely biased by the assumed under-predictions of LOS measurements. This increased complexity of the model leads to a more complete exploration of parameter space, allowing a more robust and reliable characterization of the B - n relation.

The two envelope model also has the advantage that the MAP upper envelope becomes more tightly constrained, with decreased posterior uncertainty. However, this is accompanied by an increase in the intrinsic scatter parameter, σ_B . The implication of this is that, although the model is able to characterize the large-scale trend more accurately, it attributes more of the variance in the observed B to intrinsic astrophysical scatter, rather than uncertainties in the envelope itself. As a result, the errors on individual predicted values of B are not

reduced, but may even grow, reflecting diversity in magnetic field strengths at a given density. In other words, the more robustly defined MAP line is achieved at the cost of acknowledging greater intrinsic dispersion among data points.

One of the key questions that has arisen for the B - n relation is the implied errors on n . In the original Bayesian work by C10 a fixed global error of a factor of two (equivalent to our global parameter $R = 0.30$) was used. In later work this was argued to be too small, with a value of nine being reported by Jiang et al. (2020). One of the important advantages of our new hierarchical Bayesian approach is the ability to infer a global density correction R directly from the data.

Our directly inferred R values are consistent with those found in previous studies. Across all our models and datasets, R remains modest - typically below unity and well constrained. For instance, our fiducial value for DS1, the full Zeeman data set, of $R = 0.97$ lies above the $R = 0.3$ adopted by C10, and close to the $R = 0.95$ reported by Jiang et al. (2020), and is consistent with the suggestion by Trites et al. (2015) that C10 may have underestimated the uncertainties on n . This indicates that our model retrieves a value compatible with earlier analyses, despite the difference in methodological approaches.

If our model were simply masking density scatter with flexibility in other parameters, we would expect Model B, where R is fixed, to provide a better fit with more robust posteriors at all R . However, this is not the result; Model B does not yield better-constrained or more physically plausible results. In fact, fixing R leads systemati-

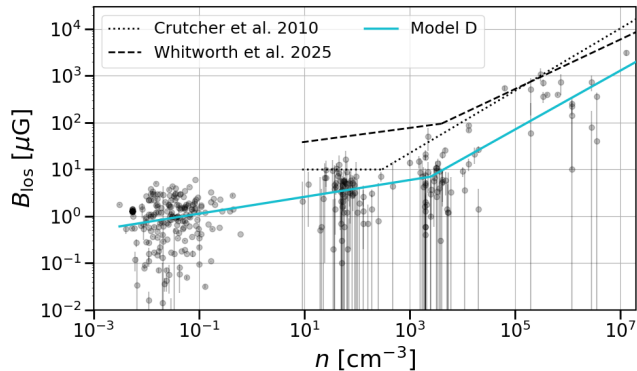


FIG. 6.— Our optimal MAP results from Model D applied to DS4 showing the new relationship we present in this work in cyan, C10 upper-limit power law (solid line) and Paper I MAP (dashed line).

cally to higher inferred break densities: for example, with a fixed value of $R = 0.3$ we obtain $n_0 \simeq 7.5 \times 10^3 \text{ cm}^{-3}$, compared to $n_0 \simeq 1.6 \times 10^3 \text{ cm}^{-3}$ when R is freely estimated in Model D ($R = 0.41$). This arises because a fixed R controls the allowed density range, forcing the model to shift n_0 to higher values in order to accommodate the high- n data. In contrast, our variable- R models A, C, and D recover R values in the range 0.4–1.1, larger than the assumption of C10, but smaller than those used by Paper I or Jiang et al. (2020). This indicates that the density correction required by the present data is modest. Part of this may reflect the heterogeneous nature of the sample itself, since the data lines of sight encompass clouds and diffuse regions that differ markedly in size, morphology, and environment, which our global approach does not take into account.

Nevertheless, understanding what drives R remains an interesting question. The balance between how density uncertainties are reported, the model’s flexibility, and the level of intrinsic physical scatter all likely influence the inferred range of R . A goal moving forward is to establish a consistent method of reporting errors on n across different datasets.

4.2. Our optimal model

We show in Appendix B that Models C and D exhibit less curved parameter degeneracies and tighter joint posteriors compared to Models A and B. Model D in particular, which incorporates the errors reported on n from the pulsar data of Seta & McClure-Griffiths (2025), provides the most reliably constrained and unimodal posteriors, so we adopt this as our benchmark model.

Examining the results for all models, it is clear that the new datasets extended to include pulsar measurements at low densities, DS3 and DS4, yield consistent trends for all error treatments and model variants. For the reasons discussed above, including the impact of the high-field outlier, we have determined that DS4 provides the best representation of the underlying B – n relationship. We therefore conclude that the most robust MAP results for each parameter come from Model D applied to DS4. We have plotted this optimal model in Figure 6 compared to the data, and provided its numerical values in Table 5.

4.3. Physical Implications

Our results reinforce those from Paper I that the magnetic field in the diffuse gas also shows variation with density, so the diffuse gas exponent α_1 should be considered as a free parameter and not set to zero. Across all four models and datasets, seen in Tables 2–5, we find that values of α_1 cluster in a narrow range around 0.2; from 0.16 in Model B DS1 with $R = 0.95$ to 0.20 in multiple models and data sets, with the exception of Model C, DS1, where α_1 is notably lower at 0.12. However, DS1 is our least favoured dataset. The value of α_1 is better constrained in the extended datasets including pulsar data, DS3 and DS4, across all models with much tighter uncertainties than in DS1 and DS2, consistent with the increased density of data at low n . This provides a narrower posterior for α_1 , reflecting increased certainty and reduced degeneracy with other parameters.

The high-density exponent α_2 shows almost no variability between models, with the only change occurring when the outlier in Sgr B2 North is removed. This is understandable, as this data point has a high field strength, $B = 460 \mu\text{G}$, for its density of $n = 5000 \text{ cm}^{-3}$, which almost always lies above the break density n_0 . Removing this point increases α_2 . With the outlier present, the model must accommodate its high field strength by flattening α_2 to avoid overpredicting B for the remaining lower-field points at high density. When it is removed, these points can be fitted with a steeper, more physically consistent α_2 .

The break density n_0 is found in the range 1000 – 4000 cm^{-3} . Models A, C, and D, where the global log density correction R is allowed to vary freely, we recover moderate values of $R \leq 1.0$ across all datasets, consistent with previous studies. In contrast, Model B, which imposes fixed R values, yields larger $n_0 = 10.02^{+0.56}_{-10.02} \times 10^3 \text{ cm}^{-3}$ for DS4 with $R = 0.70$, and even larger for $R = 0.95$. This occurs because low fixed R limits how much the true density can exceed the observed density, since $n_{\text{obs}} = n_{\text{model}} / (1 + f_n)$. Thus higher observed densities are required to reach the same model break density for the B – n relation. These results reflect differences in model assumptions rather than any fundamental discrepancy.

Our results from Models A, C, and D are broadly consistent with Paper I where $n_0 = 4.0^{13.0}_{-3.0} \times 10^3 \text{ cm}^{-3}$ is reported. As also noted in that paper, this break occurs around the point where the data becomes sparse at high densities $n = 10^4$ – 10^7 cm^{-3} . As a consequence, with the large uncertainties reported, none of the models can better constrain the value of the break density.

Physically, this transition could mark a regime where the interplay between gravity, turbulence, and magnetic fields qualitatively changes. Thus, our results suggest that it is probably not a single sharp transition but more of a change over a range of transition densities. Recent studies have suggested that at such high densities, the kinetic and turbulent energy, possibly driven by gravity, dominates over magnetic energy (Ibáñez-Mejía et al. 2022; McGuinness et al. 2026; Brucy et al. 2025). As clouds collapse to form dense cores and stars, turbulent flows amplify the magnetic field through compression of field lines and small-scale dynamo action (Seta et al. 2020). However, the density scales and specific mechanisms at play are sensitive to environmental con-

ditions such as cloud–cloud collisions and stellar feedback. Determining how n_0 varies between environments is therefore crucial, as observational constraints on n_0 will provide key tests for theoretical models of the ISM and its magnetic and turbulent energy balance.

Previous work has argued that the value $\alpha_2 \simeq 0.66$ (C10; Li et al. 2015; Jiang et al. 2020) reflects a dynamical rather than purely kinematic collapse (Mestel 1966). Our new models generally support this interpretation, although our inferred α_2 values are slightly lower and may hint at the importance of the magnetic field in slowing but not preventing dynamical collapse.

The magnetic field plays a crucial role in the formation and shaping of molecular clouds, providing magnetic support that likely increases the mass and size of the cloud (Girichidis et al. 2018; Whitworth et al. 2023; Robinson & Wadsley 2024; Pillsworth et al. 2025). However, at higher densities $n > 10^4 \text{ cm}^{-3}$ where gravitational collapse dominates, the field becomes dynamically less important relative to gravity and turbulence, whose kinetic energy may be driven by colliding flows (Brucy et al. 2025), self-gravity (Vázquez-Semadeni et al. 2019; Ibáñez-Mejía et al. 2022), or stellar feedback (Padoan et al. 2016).

4.4. Future extensions of observational data sets

Having used the pulsar data to secure a more precise value for α_1 , further improvements to our results can be made by obtaining more observational data in the higher density regime. In Figure 7, we overlay all the observational data used in this work (both Zeeman and pulsar) on the Planck all-sky map of galactic dust density. Data coverage across Quadrant 4 of the galactic plane is rather sparse.⁵ Although the combined pulsar and Zeeman data provide strong constraints on the diffuse component of the B – n relation, only 71 of the 355 data points probe regions with $n_0 > 300 \text{ cm}^{-3}$, and 67 above our new break density of $n_0 = 1630 \text{ cm}^{-3}$, likely tracing sightlines within or near the Galactic mid-plane. Expanding coverage into parts of the disk where the warm diffuse medium transitions to cold molecular gas would allow more direct constraints on n_0 . Also, additional data in the dense regime would improve constraints on α_2 .

5. CONCLUSIONS

In this work, we extended the B – n relation published in Paper I by incorporating a large set of pulsar observations (Seta & McClure-Griffiths 2025). This addition has enabled us to obtain new constraints on the exponent in the diffuse gas regime, with all our models and data sets recovering a non-zero power-law slope of $\alpha_1 \simeq 0.2$. The success of this approach stems from both the inclusion of pulsar data from Seta & McClure-Griffiths (2025), as well as a more rigorous treatment of density uncertainties through our hierarchical Bayesian framework.

Our most reliable MAP results come from Model D with Data Set 4, which combines the Zeeman measurements reported in C10 with new Zeeman data from Hwang et al. (2024) and the pulsar data, excluding the

known Zeeman outlier in Sgr B2 North. The model includes reported uncertainties on n for the low-density pulsars and allows for intrinsic variance in both n and B .

To summarize, our key results and conclusions are:

- We fit a two-part power-law to the original Zeeman data of C10 and a new extended data set that includes low-density pulsar measurements from Seta & McClure-Griffiths (2025), as well as extra Zeeman measurements from Hwang et al. (2024).
- We developed four new hierarchical Bayesian models to examine the relationship between n and B . We find that incorporating reported errors on n from the pulsar data, allowing for a global correction in n , and modelling the intrinsic scatter in B to account for geometric and observational uncertainties produces the most statistically robust results (see Appendix B for further discussion).
- The inclusion of the pulsar data in the expanded hierarchical model (Model D, DS4) yields the most robust observational B – n relation, shown in Figure 6, with MAP parameters:

$$\alpha_1 = 0.18_{-0.02}^{+0.02}, \alpha_2 = 0.63_{-0.05}^{+0.08},$$

$$n_0 = 1630_{-1430}^{+2560} \text{ cm}^{-3}, B_0 = 7.60_{-3.47}^{+2.00} \mu\text{G},$$

$$f_{B,1} = 0.80_{-0.02}^{+0.20}, f_{B,2} = 0.75_{-0.00}^{+0.23},$$

$$\sigma_B = 0.55_{-0.45}^{+0.59}, \text{ and } R = 0.42_{-0.02}^{+0.02}.$$

The large variance in n_0 may reflect the dynamical and anisotropic nature of the ISM and suggests that the transition between diffuse and dense gas likely occurs over a range of densities. Although the diffuse component of the B – n relation is now well constrained, only 67 of our 355 data points probe the dense gas. Looking ahead, expanding the observational coverage into regions where the warm diffuse medium transitions to cold molecular gas would sharpen constraints on n_0 and α_2 and advance our understanding of magnetic field dynamics across the multiphase ISM.

ACKNOWLEDGMENTS

The authors thank Sundar Srinivasan and Gwen Eadie for the original discussions on the implementation of hierarchical Bayesian techniques. We also thank Chris McKee, Edith Falgarone, and Katia Ferrière for interesting and detailed discussions on the results of Paper I. DW acknowledges support from the ANR CASCADE grant (ANR-24-ERCS-0004). AS is supported by the Australian Research Council through the Discovery Early Career Researcher Award (DECRA) Fellowship (project DE250100003) funded by the Australian Government and the Australia-Germany Joint Research Cooperation Scheme of Universities Australia (UA–DAAD, 2025–2026). REP is supported by a Discovery Grant from the Natural Sciences and Engineering Research Council (NSERC) of Canada. M-MML acknowledges partial support from US NSF grant AST23-07950. JDS acknowledges financial support from the Austrian Science Fund (Fonds zur Förderung der wissenschaftlichen

⁵ For the pulsar data coverage, see also Fig. 2 in Dhakal & Seta (2025).

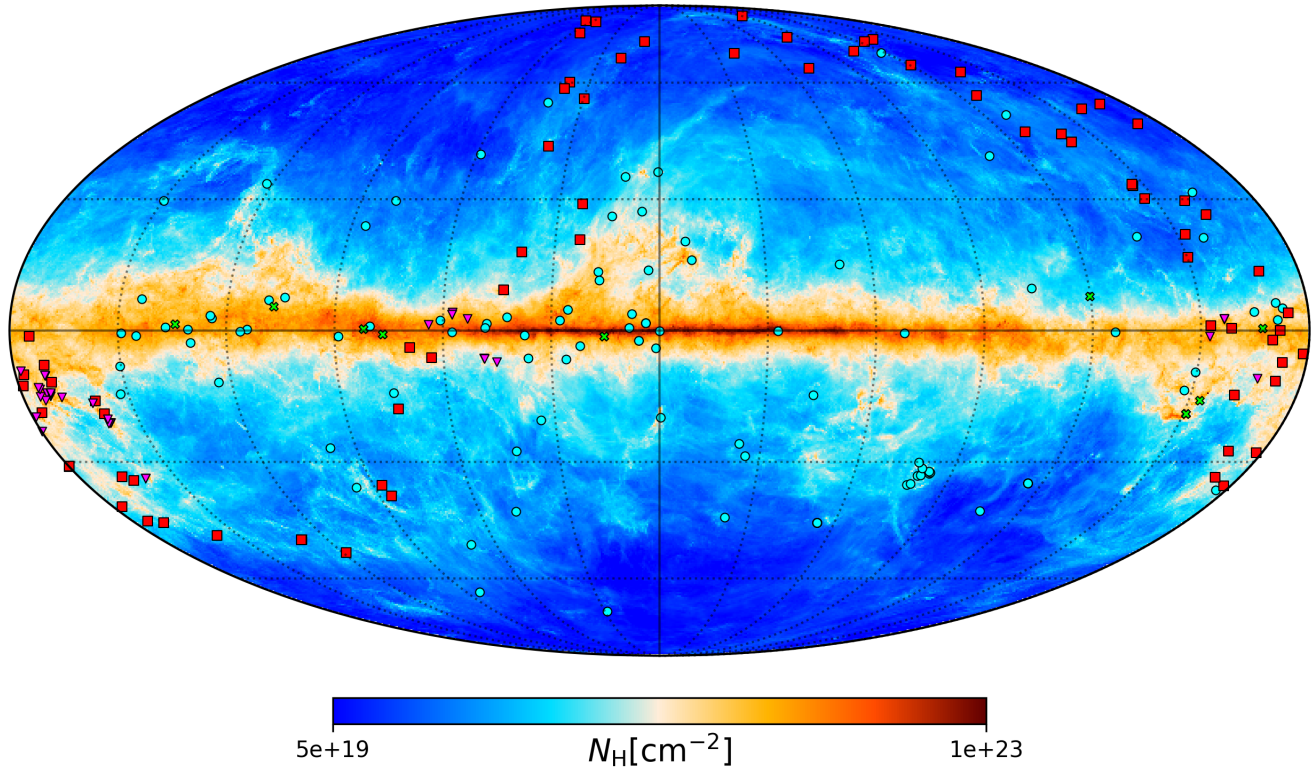


FIG. 7.— The position of observations used in this work overlaid on a Mollweide projection of dust column density derived from the *Planck* satellite observations (Planck Collaboration et al. 2016, 2020). The pulsars in Seta & McClure-Griffiths (2025) are shown as *cyan circles*. The OH Zeeman measurements from Troland & Crutcher (2008) are shown as *magenta triangles*. The CN Zeeman measurements from Falgarone et al. (2008) are *cyan crosses* and the H I Zeeman measurements from Heiles & Troland (2004) are shown as *red squares*. It can be seen that there is a lack of coverage of Quadrant 4 of the galactic plane in the observations.

Forschung, FWF) through the “Neutral Atomic Hydrogen in the solar neighborhood” (NeAtHood) project (Grant DOI 10.55776/PAT6169824). AP acknowledges financial support from the UNAM-PAPIIT IN120226 grant, and the Sistema Nacional de Investigadores de SECIHTI, México. RSK acknowledges financial support from the ERC via Synergy Grant “ECOGAL” (project ID 855130) and from the German Excellence Strategy via the Heidelberg Cluster “STRUCTURES” (EXC 2181 - 390900948). In addition, RSK is grateful for funding from the German Ministry for Economic Affairs

and Climate Action in project “MAINN” (funding ID 50002206), and from DFG and ANR for project “STAR-CLUSTERS” (funding ID KL 1358/22-1).

DATA AVAILABILITY

The hierarchical Bayesian analysis codes can be found at: https://github.com/dwhtwrth-astro/hierarchical-Bayesian_2026.git whilst the data can be found in either the relevant papers or through contacting their authors.

REFERENCES

- Angarita Y., Versteeg M. J. F., Haverkorn M., Marchal A., Rodrigues C. V., Magalhães A. M., Santos-Lima R., Kawabata K. S., 2024, *AJ*, 168, 47
- Beck R., 2015, *A&A Rev.*, 24, 4
- Betancourt M., 2017, arXiv preprint arXiv:1701.02434
- Bogue K. R. J., et al., 2026, *MNRAS*, 545, staf2132
- Brucy N., Vázquez-Semadeni E., Colman T., Fensch J., Klessen R. S., 2025, arXiv e-prints, p. arXiv:2510.09480
- Chen C.-Y., Li Z.-Y., Mazzei R. R., Park J., Fissel L. M., Chen M. C. Y., Klein R. I., Li P. S., 2022, *MNRAS*, 514, 1575
- Ching T.-C., Li D., Heiles C., Li Z.-Y., Qian L., Yue Y. L., Tang J., Jiao S. H., 2022, *Nature*, 601, 49
- Crutcher R. M., 2012, *ARA&A*, 50, 29
- Crutcher R. M., Wandelt B., Heiles C., Falgarone E., Troland T. H., 2010, *ApJ*, 725, 466
- Dhakal S., Seta A., 2025, *MNRAS*, 544, 2698
- Edenhofer G., Zucker C., Frank P., Saydjari A. K., Speagle J. S., Finkbeiner D., Enßlin T. A., 2024, *A&A*, 685, A82
- Falgarone E., Troland T. H., Crutcher R. M., Paubert G., 2008, *A&A*, 487, 247
- Ferrière K., 2020, *Plasma Physics and Controlled Fusion*, 62, 014014
- Fiege J. D., Pudritz R. E., 2000, *MNRAS*, 311, 85
- Gelman A., Rubin D. B., 1992, *Statistical Science*, 7, 457
- Gent F. A., Mac Low M.-M., Korpi-Lagg M. J., 2023, arXiv e-prints, p. arXiv:2306.07051
- Girichidis P., Seifried D., Naab T., Peters T., Walch S., Wünsch R., Glover S. C. O., Klessen R. S., 2018, *MNRAS*, 480, 3511
- Han J. L., 2017, *ARA&A*, 55, 111
- Heiles C., Crutcher R., 2005, in Wiebeinski R., Beck R., eds, , Vol. 664, *Cosmic Magnetic Fields*. Springer, p. 137, doi:10.1007/3540313966_7
- Heiles C., Troland T. H., 2004, *ApJS*, 151, 271
- Hennebelle P., Inutsuka S.-i., 2019, *Frontiers in Astronomy and Space Sciences*, 6, 5
- Hewish A., Bell S. J., Pilkington J. D. H., Scott P. F., Collins R. A., 1968, *Nature*, 217, 709

Hwang J., Lee C. W., Kim J., Chung E. J., Kim K.-T., 2024, *ApJ*, **974**, 231
 Ibáñez-Mejía J. C., Mac Low M.-M., Klessen R. S., 2022, *ApJ*, **925**, 196
 Jiang H., Li H.-b., Fan X., 2020, *ApJ*, **890**, 153
 Koley A., Roy N., Menten K. M., Jacob A. M., Pillai T. G. S., Rugel M. R., 2021, *MNRAS*, **501**, 4825
 Leroy A. K., et al., 2017, *ApJ*, **846**, 71
 Li P. S., McKee C. F., Klein R. I., 2015, *MNRAS*, **452**, 2500
 Manchester R. N., 1974, *ApJ*, **188**, 637
 Manchester R. N., Hobbs G. B., Teoh A., Hobbs M., 2005, *AJ*, **129**, 1993
 McGuinness R., Smith R. J., Whitworth D., 2026, *MNRAS*, **546**, *stag099*
 Mestel L., 1966, *MNRAS*, **133**, 265
 Mestel L., Spitzer Jr. L., 1956, *MNRAS*, **116**, 503
 Metropolis N., Rosenbluth A. W., Rosenbluth M. N., Teller A. H., Teller E., 1953, *J. Chem. Phys.*, **21**, 1087
 Mouschovias T. C., 1976, *ApJ*, **207**, 141
 Nakamura F., Kamenno S., Kusune T., Mizuno I., Dobashi K., Shimoikura T., Taniguchi K., 2019, *PASJ*, **71**, 117
 Nakano T., 1973, *PASJ*, **25**, 91
 Neal R., 2011, in *Handbook of Markov Chain Monte Carlo*. Chapman and Hall/CRC, pp 113–162, [doi:10.1201/b10905](https://doi.org/10.1201/b10905)
 Padoan P., Pan L., Haugbølle T., Nordlund Å., 2016, *ApJ*, **822**, 11

APPENDIX APPENDIX 1

Whilst developing the hierarchical Bayesian models used in this work, we identified and corrected an implementation error in the original code used by [Paper I](#) that affected the inferred value of B_0 . Specifically, a duplicate prior sampling statement on σ_y in the HMC model overweighted the prior distribution on intrinsic scatter, which contributed to biasing the inferred value of B_0 . Correcting this error motivated further improvements to the statistical framework. Following the approach of [Jiang et al. \(2020\)](#), we introduced an envelope scaling factor f_B to account for projection effects. We also replaced the individual latent density values for each observation with a single global correction parameter f_n .

To assess the impact of these combined changes, we tested the extended Zeeman plus pulsar dataset DS4 using both the original code and our new implementation. [Table A1](#) shows the results from this test compared to the results for Models A, C, and D, and plotted in [Figure A1](#). The comparison reveals that B_0 is systematically overpredicted in the original code by factors of ~ 2 – 10 depending on the model, whilst the power-law indices α_1 and α_2 and density break-point n_0 remain relatively stable across implementations.

The physical significance becomes evident when examining our more sophisticated Models C and D. Using the corrected implementation and improved modelling, B_0 converges to $\sim 8 \mu\text{G}$, close to the Milky Way’s average magnetic field strength and the originally reported value of $10 \mu\text{G}$ in [C10](#). This convergence demonstrates that our improved hierarchical framework more accurately captures the underlying B – n relationship.

APPENDIX 2

Here we present the corner plots for DS4 for our models. For Model B, we show only the case with $R = 2$.

Pattle K., Fissel L., Tahani M., Liu T., Ntormousi E., 2023, in *Inutsuka S., Aikawa Y., Muto T., Tomida K., Tamura M.*, eds, *Astronomical Society of the Pacific Conference Series Vol. 534, Protostars and Planets VII*. p. 193 ([arXiv:2203.11179](https://arxiv.org/abs/2203.11179)), [doi:10.48550/arXiv.2203.11179](https://doi.org/10.48550/arXiv.2203.11179)
 Pillsworth R., Roscoe E., Pudritz R. E., Koch E. W., 2025, *ApJ*, **987**, 20
 Pineda J. L., Goldsmith P. F., Chapman N., Snell R. L., Li D., Cambrésy L., Brunt C., 2010, *ApJ*, **721**, 686
 Planck Collaboration Ade P. A. R., et al. 2016, *A&A*, **586**, A138
 Planck Collaboration Aghanim N., et al. 2020, *A&A*, **641**, A1
 Robinson H., Wadsley J., 2024, *MNRAS*, **534**, 1420
 Seta A., Federrath C., 2021, *MNRAS*, **502**, 2220
 Seta A., Federrath C., 2022, *MNRAS*, **514**, 957
 Seta A., McClure-Griffiths N. M., 2025, *MNRAS*, **539**, 1024
 Seta A., Bushby P. J., Shukurov A., Wood T. S., 2020, *Physical Review Fluids*, **5**, 043702
 Smith F. G., 1968, *Nature*, **220**, 891
 Soler J. D., et al., 2025, *A&A*, **695**, A222
 Thompson K. L., Troland T. H., Heiles C., 2019, *ApJ*, **884**, 49
 Tritsis A., Panopoulou G. V., Mouschovias T. C., Tassis K., Pavlidou V., 2015, *MNRAS*, **451**, 4384
 Troland T. H., Crutcher R. M., 2008, *ApJ*, **680**, 457
 Vázquez-Semadeni E., Palau A., Ballesteros-Paredes J., Gómez G. C., Zamora-Avilés M., 2019, *MNRAS*, **490**, 3061
 Whitworth D. J., Smith R. J., Klessen R. S., Mac Low M.-M., Glover S. C. O., Tress R., Pakmor R., Soler J. D., 2023, *MNRAS*, **520**, 89
 Whitworth D. J., et al., 2025, *MNRAS*, **540**, 2762
 Zucker C., et al., 2021, *ApJ*, **919**, 35

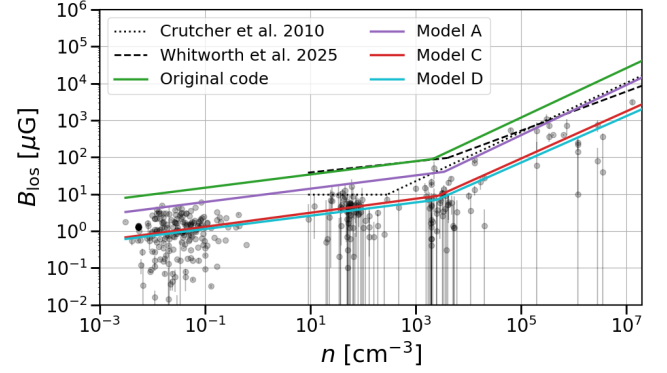


FIG. A1.— A comparison between the code from [Paper I](#), applied to DS4, and the code used in this paper for Models A, C, and D. We see that the original incorrect code overpredicts the value for B_0 .

TABLE A1
COMPARISON BETWEEN RESULTS IN [PAPER I](#) AND NEW MODELS

	α_1	α_2	n_0 , (10^3cm^{-3})	B_0 , (μG)
Paper I	$0.19^{+0.02}_{-0.02}$	$0.67^{+0.08}_{-0.07}$	$1.10^{+2.00}_{-0.80}$	$81.0^{+33.0}_{-22.0}$
Model A	$0.18^{+0.02}_{-0.02}$	$0.68^{+0.04}_{-0.11}$	$2.45^{+1.35}_{-2.45}$	$39.90^{+7.80}_{-36.60}$
Model C	$0.19^{+0.02}_{-0.02}$	$0.64^{+0.06}_{-0.07}$	$2.66^{+1.23}_{-2.66}$	$8.66^{+0.76}_{-4.41}$
Model D	$0.18^{+0.02}_{-0.02}$	$0.63^{+0.08}_{-0.05}$	$1.63^{+2.56}_{-1.46}$	$7.60^{+2.00}_{-3.37}$

Notes. A comparison between the code from [Paper I](#) and the revised code used in this paper for Models A, C, and D, all applied to DS4.

Models A and B (Figures B1 and B2) exhibit broader and more skewed posteriors, with mild hints of bi-modality, particularly in $\log_{10} n_0$, where a small secondary peak is visible, and possibly in α_1 . Model C (Figure B3) shows nearly Gaussian joint distributions, though weak bi-modality remains in $\log_{10} n_0$ and $\log_{10} B_0$, having mostly disappeared for α_1 . Model D (Figure B4) exhibits unimodal, approximately Gaussian posteriors for all parameters, with only slight elliptical covariance and no strong degeneracies.

The sharp upper limits seen in f_B , $f_{B,1}$, and $f_{B,2}$ for Models A, C, and D arise from how this parameter is implemented in the Bayesian framework. The prior on each is defined over $\log_{10} f_B$ between 0 and 1 (see Table 1), and because it enters the model as an additive term in Equation (5), the allowed range enforces $f_B \leq 1$. In

Models C and D, where separate scaling factors $f_{B,1}$ and $f_{B,2}$ are used above and below the break density n_0 , both parameters tend to saturate at the upper bound of 1, indicating that the data prefer minimal suppression of B relative to B_0 in both regimes. In contrast, Model A employs a single scaling factor over the full dataset, and its posterior for f_B is correspondingly broader, reflecting the need to accommodate the full density range within one scaling parameter supporting our choice of Model D for our most robust result.

This paper was built using the Open Journal of Astrophysics L^AT_EX template. The OJA is a journal which provides fast and easy peer review for new papers in the `astro-ph` section of the arXiv, making the reviewing process simpler for authors and referees alike. Learn more at <http://astro.theoj.org>.

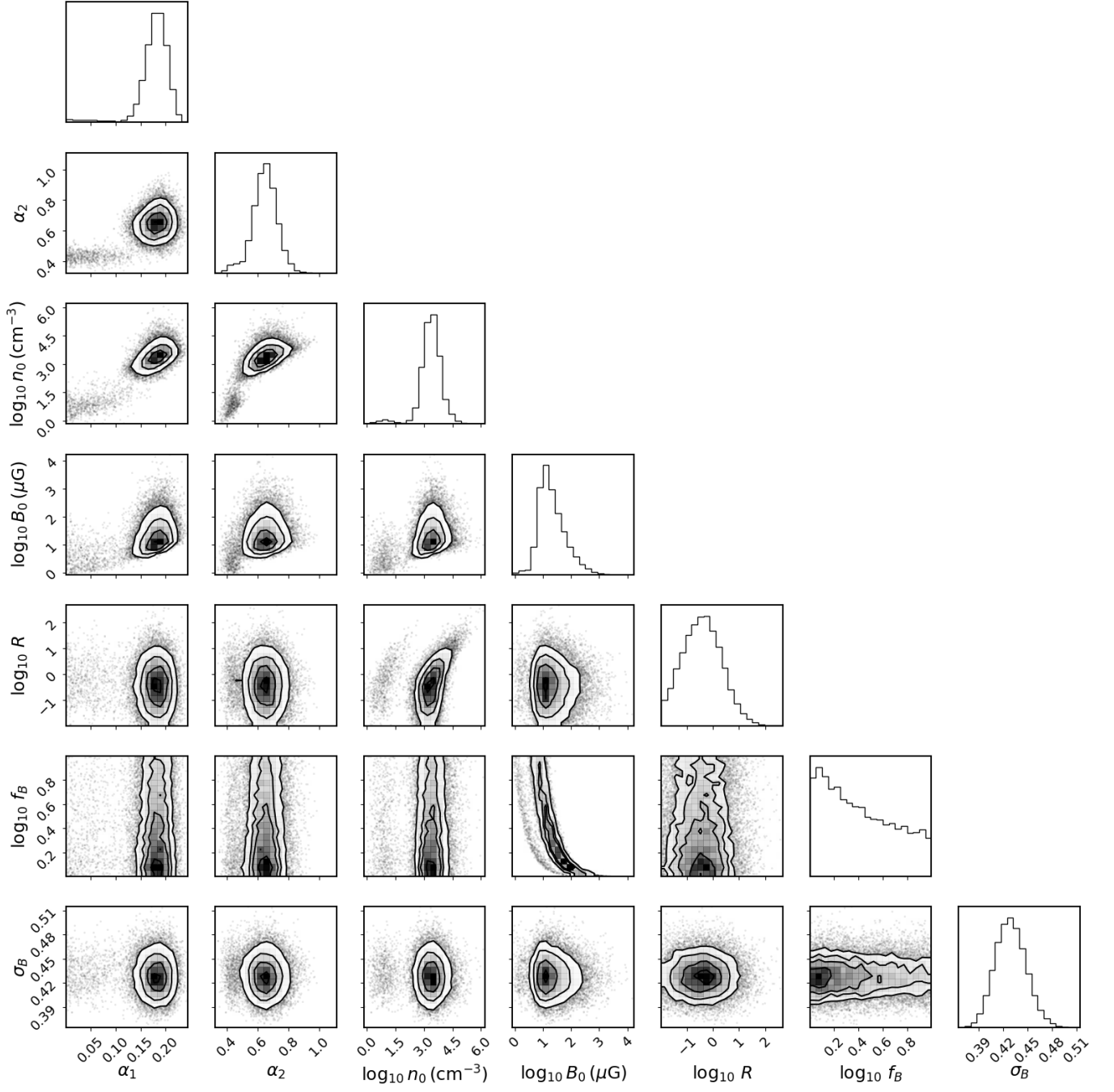


FIG. B1.— Corner plot for Model A applied to DS4

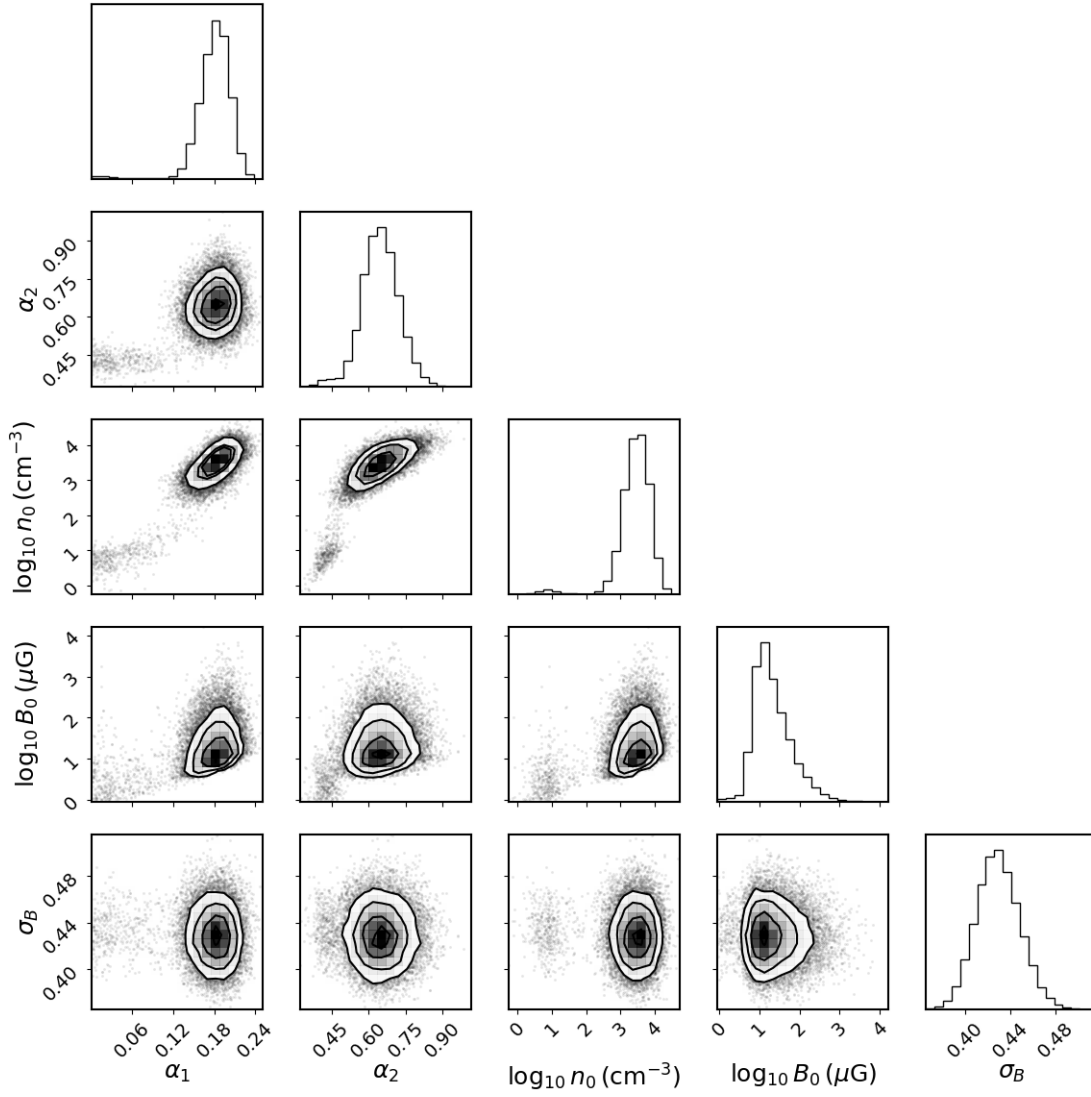


FIG. B2.— Corner plot for $R = 2$ for Model B applied to DS4

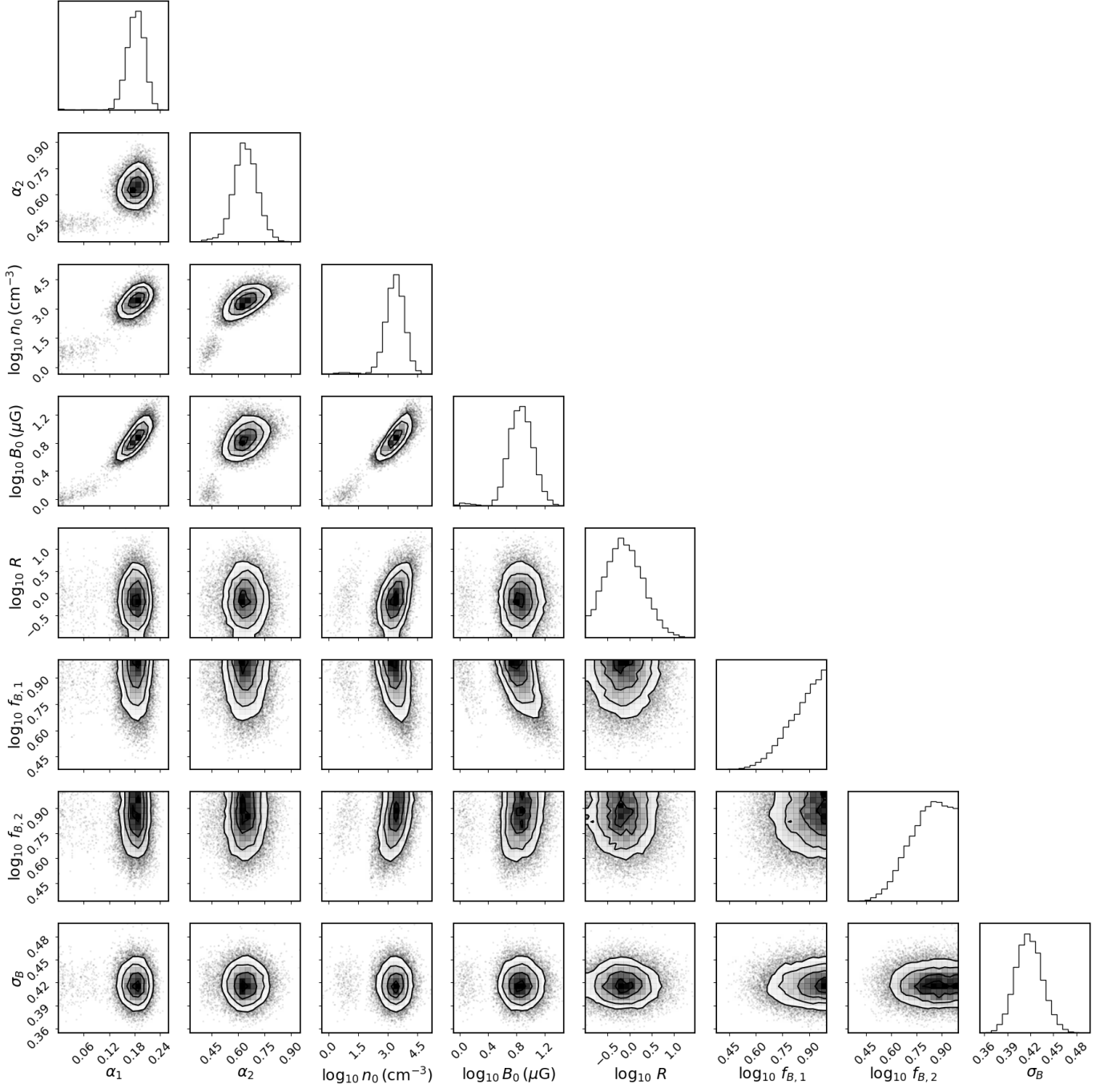


FIG. B3.— Corner plot for Model C applied to DS4

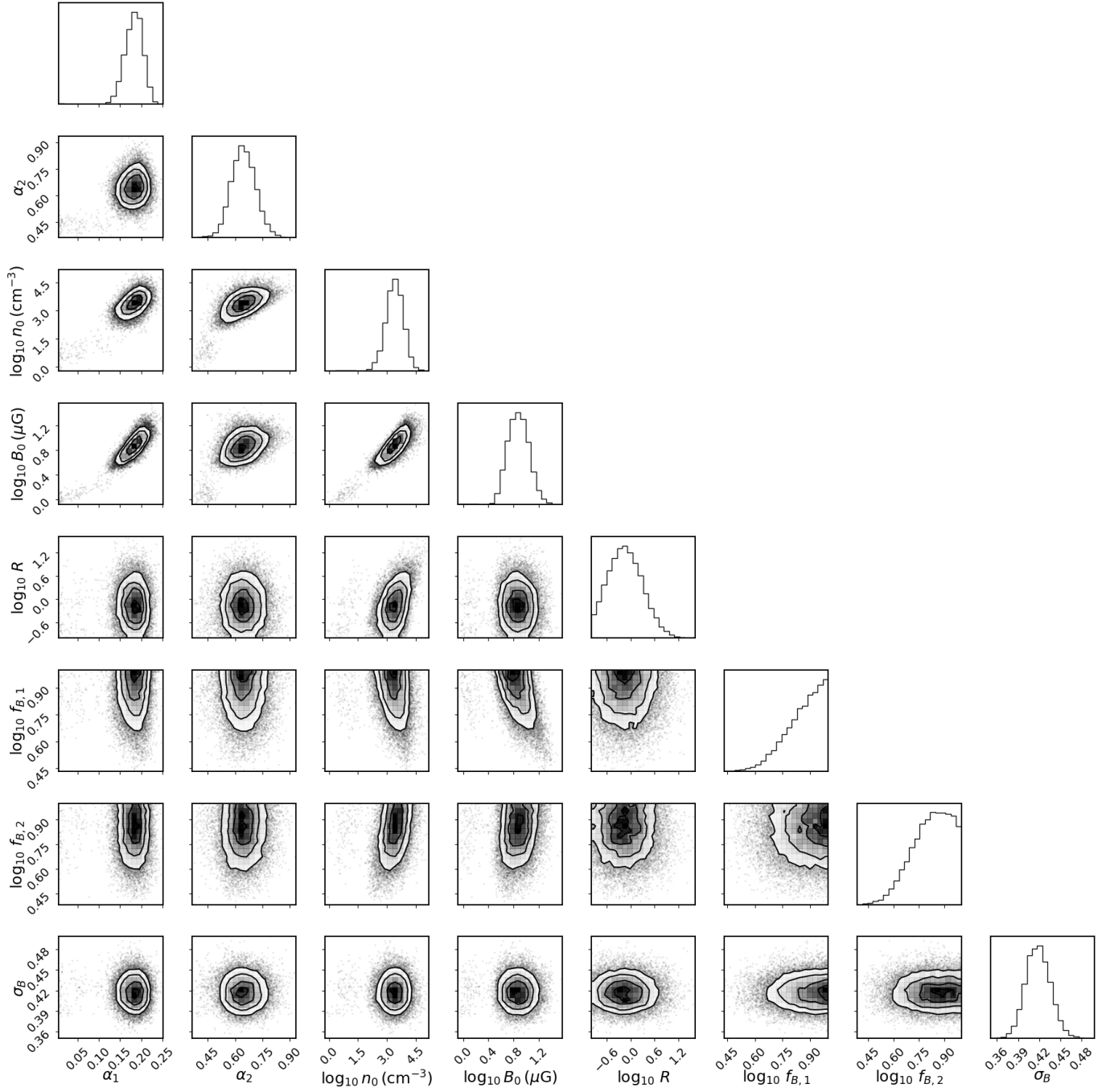


FIG. B4.— Corner plot for Model D applied to DS4